

MDPI

Article

Repair of Gear by Laser Cladding Ni60 Alloy Powder: Process, Microstructure and Mechanical Performance

Chuang Guan 1,2,3, Tianbiao Yu 1,*, Yu Zhao 4, Liaoyuan Chen 1 and Ying Chen 1

- ¹ School of Mechanical Engineering and Automation, Northeastern University, Shenyang 110819, China
- National Frontiers Science Center for Industrial Intelligence and Systems Optimization, Shenyang 110819, China
- ³ Key Laboratory of Date Analytics and Optimization for Smart Industry (Northeastern University), Ministry of Education, Shengyang 110819, China
- ⁴ School of Mechanical and Aerospace Engineering, Jilin University, Changchun 130025, China
- * Correspondence: tianbiaoyudyx@gmail.com

Abstract: As the main mechanical transmission parts, the gears are usually exposed to wear, corrosion, and fatigue; their failure in a poor working environment may cause a huge economic loss and waste of resources. Laser cladding (LC) has been proven to quickly repair parts at good metallurgical bonding performance and has flexible scanning strategies and a wide material selection. Therefore, LC technology can be considered an ideal approach to repairing damaged gear. However, the repair of damaged teeth by LC has not been systematically reported. In this paper, a series of progressive works have been carried out to systematically investigate the repair process of broken gears by LC. Firstly, process parameters, overlapping ratio, and Z-increment for Ni60 powder on 20CrMnTi were optimized. Secondly, the effects of deposition strategies on morphologies of single-layer and multi-layer multi-tracks were carefully analyzed. Then, the gear repair was successfully realized based on obtained optimized parameters. Finally, the phase composition, microstructure, hardness, and wear properties of the repaired gear tooth were analyzed by XRD, SEM, microhardness tester, and friction and wear tester. The results show that the remanufactured tooth can recover its appearance before breakage. The repaired zone is mainly composed of γ -Ni, Cr_7C_3 , $Cr_{23}C_6$, and CrB phases. The micro-hardness and wear volume loss of the repaired zone is 60.63 ± 1.23 HRC and $1674.983 \mu m^2$, which are consistent with those of the other teeth. This study is expected to expand the application of LC technology and provide guidance to engineers in the repair of damaged parts.

Keywords: laser cladding; Ni60 powder; repairing damaged gear; microstructure; microhardness; wear resistance



Citation: Guan, C.; Yu, T.; Zhao, Y.; Chen, L.; Chen, Y. Repair of Gear by Laser Cladding Ni60 Alloy Powder: Process, Microstructure and Mechanical Performance. *Appl. Sci.* **2023**, *13*, 319. https://doi.org/ 10.3390/app13010319

Academic Editor: Abílio Manuel Pinho de Jesus

Received: 22 November 2022 Revised: 14 December 2022 Accepted: 21 December 2022 Published: 27 December 2022



Copyright: © 2022 by the authors. Licensee MDPI, Basel, Switzerland. This article is an open access article distributed under the terms and conditions of the Creative Commons Attribution (CC BY) license (https://creativecommons.org/licenses/by/4.0/).

1. Introduction

Gears, as the main transmission parts, can bear alternating stress, heavy load, and the impact load effect. Bad working conditions result in gear surface transition wear, which frequently produces excessive noise and vibration. The vibration could lead to unstable transmission and thus reduce transmission accuracy. In serious cases, it would lead to a scrap of gear [1,2]. The machine tool gear market alone has an inventory of about eight million units in China, ranking several years in a row as the world's first in number. Among them, there are more than 2.2 million traditional machine tools that have been in service for more than 14 years. A total of 80% of the machine tools are in overtime service. For the repair of used and scrap machine tools, the spindle, gear, guide rail, and main axle box of the machine tools can be used as recycling. The recycling utilization rate of machine parts is above 85%, which can save more than 80% of the energy compared with the repair of new machine tools [3]. Due to environmental protection, transmission importance, high utilization, saving resources, special geometry, and high cost of gears, the repair of gears is a problem that has concerned a lot of scholars.

Appl. Sci. 2023, 13, 319 2 of 22

Laser cladding (LC) has been applied in various fields [4–7]. LC is mainly applied to repair and surface strengthening in the fields of aerospace, automotive, petrochemical, metallurgy, and rail transportation. It provides a new option to repair damaged parts, especially important parts, greatly reducing cost and enhancing work efficiency [8]. LC repair technology is a kind of remanufacturing technology, which repairs damaged parts and components using reverse engineering and powder-feed additive manufacturing [9,10]. LC repair has multiple advantages: low heat input leads to low distortion and low thermal damage in the base substrate, wide material applicability, rapid response to market demand, and a finer microstructure achieved, compared to arc welding, cold spray, and plasma spray [11–14]. LC repair is regarded as a prospective technology reducing the environmental impact of products by extending their lifespan rather than replacing them.

Until now, LC repair technology has gradually been widely applied in different industrial fields. The damaged wheel was repaired by LC. The life evaluation models for repair wheels were established, and the existing railroad wheel damage assessment model was improved. It provides a new idea for the application and maintenance of railroad wheels [15]. The effect of the additive powders B₄C and Ti on the damaged carbon steel was studied by adjusting their ratios to obtain mechanical properties with refined organization and good bonding with the substrate. Research shows that 5B₄C and the 15Ti (in wt.%) powder can obtain better morphology, phase composition, microstructure, and mechanical properties [16]. The Ni45 powder was selected to repair 45 steel gear. The laser beam enters from the midpoint of two roots to solve the problem of difficult machining of complex shapes. The hardness and wear resistance of the cladding layer is analyzed to determine that the performance of the cladding layer is better than that of the substrate. However, the optimization of the whole process system is not introduced in detail [1]. A new non-dominated sorting genetic algorithm ii (NSGA-II) to solve the repair model of LC is proposed. The improved TOPSIS sorting and optimization technology was adopted, and the optimal process parameters were obtained. The remanufacturing experiment verifies that the optimized parameters meet the experimental requirements and verify the model and algorithm can effectively reduce the energy consumption of the laser remanufacturing process [17]. Kf311ferrous metal powder was chosen to repair steel EA4T by LC. The study has shown that smaller grain size and the precipitation of Fe₂B phases caused by remelting and recrystallization of alloying powder lead to the highest microhardness value of cladding layers [18]. Laser cladding technology was used on the wind power gearbox spline shaft. The Fe-based coatings with different WC addition were manufactured by laser cladding to improve the wear resistance of the wind turbine gears, increasing microhardness and wear resistance with increasing WC content in ironbased coatings [19]. Although some scholars have conducted some research on deposition strategy and parameter optimization, their research studies are incomplete. The whole repair process has not formed a system. Because of the complex morphology and the high height of the deposition layer to be repaired, the requirements for the deposition strategy are higher. In this study, the systematic research combination of process parameters' optimization, deposition strategy optimization, microstructure analysis, and mechanical properties are studied in depth. The above scholars have studied the repair of the wheel, gear, and even damaged substrates, but the repair scope is relatively small, and there is no study on the large-scale deposition layer with complex morphology with high hardness. Some studies are not targeted, such as considering the substrate as a broken part. This paper makes up for the deficiency in this respect.

In this paper, to ensure mechanical performance, Ni60 power was chosen as the LC powder. The process parameters' optimization, deposition strategy determination, microstructure analysis, mechanical properties detection, and analysis of high hardness 20CrMnTi gear tooth surface restoration were systematically studied. The optimal process parameters include powder feeding rate (V_p) , laser power (P), scanning speed (V_s) , carrier gas flow rate (Q), overlap rate, and Z-axis increment. The deposition strategy includes scanning mode, the lap mode of the track, and the way of the lap between layers. Phase and

Appl. Sci. 2023, 13, 319 3 of 22

microstructure analysis, microhardness test, and wear performance were systematically investigated to improve the surface quality. Finally, the gear tooth was repaired successfully, and the properties of the repair part were similar to those of the original gear.

2. Experimental Procedure

2.1. Materials and Experimental Set-Up

In this work, Ni60 alloy powder was chosen to repair the worn tooth of 20CrMnTi super gear owing to their similar hardness and melting point. Moreover, Ni60 alloy powder has excellent self-fluxing, high tenacity, good resistance, and good antioxidant activity [20,21]. The shape of Ni60 powder with a size of 100–270 mesh is nearly a sphere, as shown in Figure 1a. The size of Ni60 powder is 38.98–118.69 μ m, and the average size is 77.53 μ m, as shown in Figure 1b. The powder particle size is measured using the software of image-pro plus. Table 1 lists the main mass chemical composition of Ni60 and 20CrMnTi.

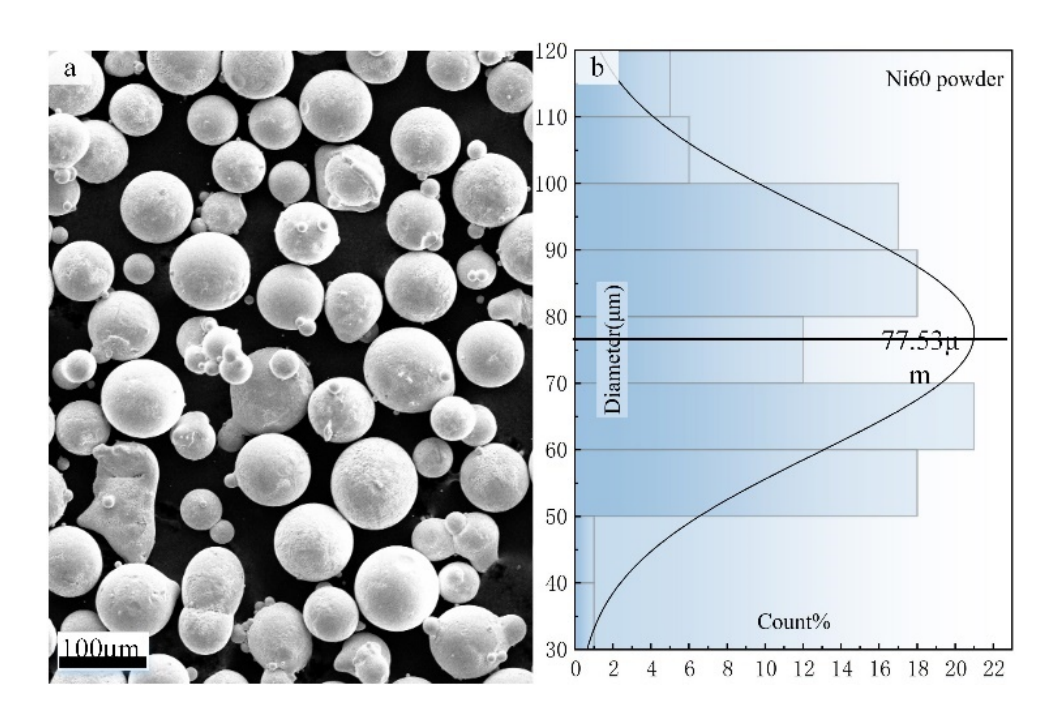


Figure 1. SEM image of Ni60 alloy powder: (a) geometry shape of Ni60, (b) size statistic of Ni60.

Table 1. The com	ponent of Ni60 ar	nd 20CrMnTi (wt. %).	

Element	С	Si	Mn	Cr	Ni	В	Fe
20CrMnTi	0.17-0.23	0.17-0.37	0.80-0.10	1.00-1.30	≤0.030	-	Bal.
Ni60	0.5	4.5	-	1.8	Bal.	3	15

The LC system for the experiment is composed of the laser head, 6-axis KUKA robot, powder feeder, laser generator, water cooler, robot control system, and control cabinet, as shown in Figure 2. IPG YLR-500 fiber laser is employed to generate the laser beam, the wavelength of the laser beam is 1070 nm, and the maximum power is 500 W.

Appl. Sci. 2023, 13, 319 4 of 22

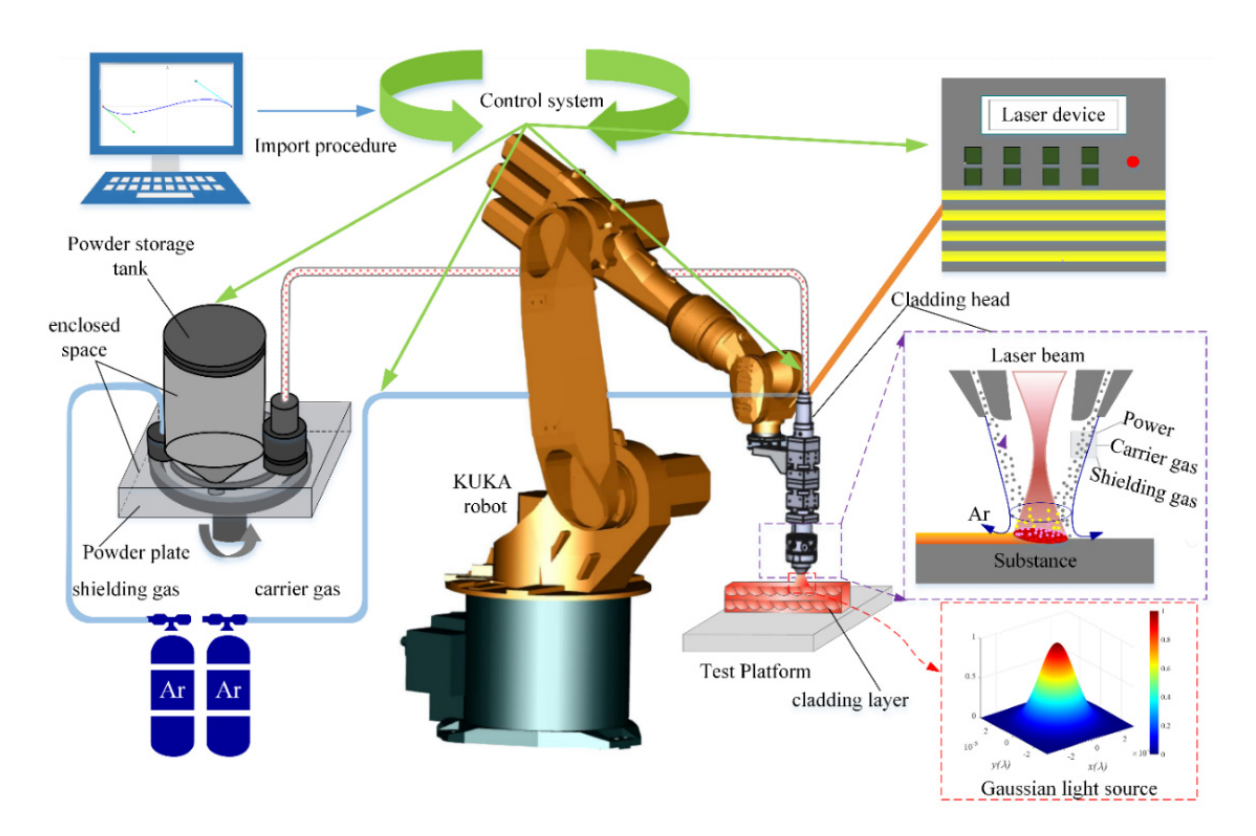


Figure 2. The schematic diagram of the LC experiment device.

2.2. Laser Repairing Process

2.2.1. Parameter Optimization

The geometry characteristics of the clad track are strongly influenced by the process parameters, as reported in [22,23]; among them, the dilution ratio β (the ratio of depth (h) and overall height (H + h)) is directly affected by the quality of longitudinal lap as Equation (1) [24]; the aspect ratio λ (the ratio of width (W) and height (H)) are directly determined by the quality of transverse lap as Equation (2) [25]. S_m and S_c in Equation (1) represent the melt pool area and the cladding layer area, respectively. Geometry characteristics are shown in Figure 3. The process parameters of LC, including powder feeding rate (V_p) , laser power (P), scanning speed (V_s) , and carrier gas rate (Q), are crucial for the geometry characteristics of LC coating [26–28]. Therefore, the four parameters were chosen as the key factors to find empirical-statistical correlations between the process parameters and geometrical characteristics. The four-parameter ranges were selected based on the parameters of existing experimental equipment and previous studies of the same equipment [16,29,30]. The dilution ratio β and aspect ratio λ was expected to predict the geometric characteristics. To select the ideal process parameters for the LC Ni60 alloy powder on 20CrMnTi substrate, a single-track orthogonal experiment and an interactive experiment were designed, as shown in Tables 2 and 3.

$$\beta = \frac{S_m}{S_m + S_c} \approx \frac{h}{h + H} \tag{1}$$

$$\lambda = \frac{W}{H} \tag{2}$$

Appl. Sci. 2023, 13, 319 5 of 22

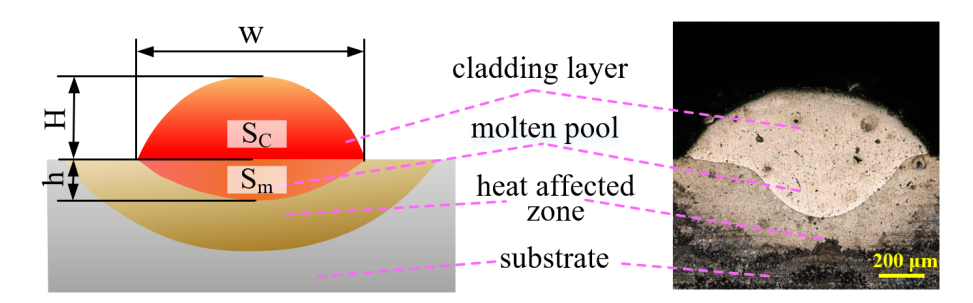


Figure 3. LC morphology of single channel and geometric feature.

Table 2. Design and results of the orthogonal experiment.

No.	P (W)	Vs (mm/s)	Vp (r/min)	Q (L/min)	β	W/H
1	360	6	0.4	8	0.4758	4.1131
2	360	8	0.6	7	0.1854	3.1586
3	360	10	0.8	6	0.0354	2.1342
4	380	6	0.4	7	0.1614	2.6136
5	380	8	0.6	6	0.0379	2.0102
6	380	10	0.8	8	0.4726	5.5973
7	400	6	0.6	8	0.4946	3.8984
8	400	8	0.8	7	0.2417	3.2292
9	400	10	0.4	6	0.0530	2.1473
10	360	6	0.8	6	0.4246	8.9034
11	360	8	0.4	8	0.4750	4.0557
12	360	10	0.6	7	0.1704	3.7500
13	380	6	0.6	6	0.5142	11.4234
14	380	8	0.8	8	0.3222	4.4295
15	380	10	0.4	7	0.2200	3.4587
16	400	6	0.8	7	0.1861	2.4811
17	400	8	0.4	6	0.6854	18.1548
18	400	10	0.6	8	0.4078	5.3525

Table 3. Design and results of interaction experiment.

No.	Q	V_S	$Q imes V_S$	P	$Q \times P$	$V_S imes P$	V_P	$Q \times V_P$	$V_S imes V_P$	$P \times V_P$	β
1	7	8.5	1	370	1	1	0.60	1	1	1	0.342
2	7	8.5	1	370	1	1	0.70	2	2	2	0.298
3	7	8.5	1	380	2	2	0.60	1	1	2	0.308
4	7	8.5	1	380	2	2	0.70	2	2	1	0.351
5	7	9.5	2	370	1	2	0.60	1	2	1	0.289
6	7	9.5	2	370	1	2	0.70	2	1	2	0.287
7	7	9.5	2	380	2	1	0.60	1	2	2	0.297
8	7	9.5	2	380	2	1	0.70	2	1	1	0.301
9	7.5	8.5	2	370	2	1	0.60	2	1	1	0.187
10	7.5	8.5	2	370	2	1	0.70	1	2	2	0.165
11	7.5	8.5	2	380	1	2	0.60	2	1	2	0.207
12	7.5	8.5	2	380	1	2	0.70	1	2	1	0.190
13	7.5	9.5	1	370	2	2	0.60	2	2	1	0.205
14	7.5	9.5	1	370	2	2	0.70	1	1	2	0.170
15	7.5	9.5	1	380	1	1	0.60	2	2	2	0.240
16	7.5	9.5	1	380	1	1	0.70	1	1	1	0.264

2.2.2. Overlap Rate and Z-Increments Optimization

The overlapping ratio, which includes the transverse overlapping ratio (δ) and longitudinal overlapping ΔZ , is shown in Figure 4a. The pores or less filled zone would appear in the cladding layer when δ is too small. However, when δ is too large, the material accumulation would occur, which reduces the deposition rate. Theoretical δ can be defined

Appl. Sci. 2023, 13, 319 6 of 22

by Equations (3) and (4) [31]. According to orthogonal results, the average value of the cladding layer width of 18 tracks is 1.4 mm. Therefore, the distance (D_1) between two adjacent tracks should be less than 1.4 mm. The laser spot diameter (d) is 1.0 mm, so the D_1 should not be small. The D_1 is selected as 0.6, 0.8, 1.0, 1.2, and 1.4 mm, respectively:

$$W \ge D_1 \tag{3}$$

$$\delta = \frac{D_0}{W} = \frac{W - D_1}{W} \tag{4}$$

where D_0 is the length of overlapping.

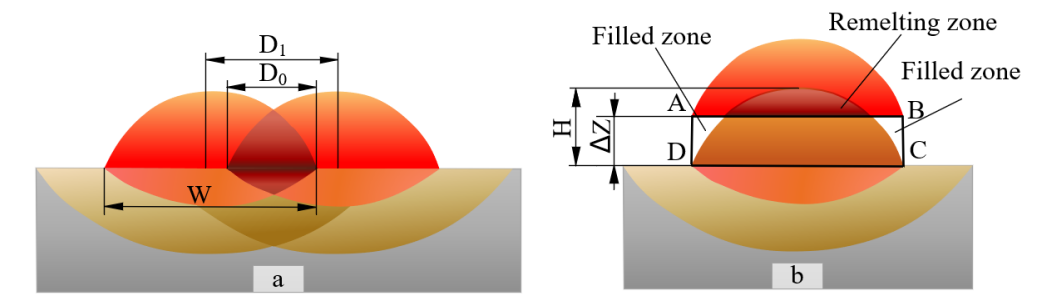


Figure 4. Schematic diagram of lapping model: (a) transverse overlapping, (b) longitudinal overlapping.

For longitudinal overlapping (z-increment), a part of the liquid metal in the second layer would spread to both sides under the effect of surface tension and gravity, as Figure 4b. When the remelting zone is equal to the filled zone of the peripheral generation, a relatively flat surface can be obtained. Under this premise, the area of quadrilateral ABCD should be equal to the cross-section area of the cladding track. After n-layer LC, the total height is defined as H_T , and $H_T = (n-1) \Delta Z + H$. The ΔZ is calculated by Equation (5) [25]. However, considering the errors between the theory and experiment, three groups of experiments are designed, and the ΔZ was set as 0.30, 0.28, and 0.26 mm, respectively:

$$\Delta Z = \frac{(4H^2 + W^2)^2}{64H^2W} \arcsin(\frac{4WH}{4H^2 + W^2}) - \frac{W(W^2 - 4H^2)}{16H}$$
 (5)

where W is approximately 1.4 mm, H stands for the average value of the cladding height of 18 tracks, and H = 0.394 mm.

2.2.3. Deposition Strategies Optimization

Figure 5 shows the three different lapping strategies. When the first path is finished, the adjacent path is directly LC. During this process, the first path does not have enough time to cool, so strategy I-1 is defined as a hot lap joint. In contrast to the hot lap, the traditional cold lap has enough time to cool between the first path and the second path, but the second path has no time to cool according to deposition strategy I-2, failing to fully reflect the role of the cold lap. This paper studies a lap way named optimized cold strategy, as shown in Figure 5(I-3). Moreover, two scanning modes on a single layer were adopted: co-directional scanning (Figure 5(II-1)) and reverse scanning (Figure 5(II-2)), where the thick line path with arrowheads is a laser beam scanning route, and the fine line path with arrowhead is a powder scanning route. Before conducting the repair gear tooth experiment, the deposition strategies were designed. Three kinds of multi-channel strategies have been carried out to fabricate the gear tooth, respectively. The deposition strategies are shown in Figure 5(III-1–III-3). For strategy III-1, the scanning directions of each layer are perpendicular to the axial direction of the gear. For strategy III-2, the scanning directions of each layer are parallel to the axial direction of the gear. For strategy III-3, the scanning directions of the two adjacent layers are perpendicular to each other.

Appl. Sci. 2023, 13, 319 7 of 22

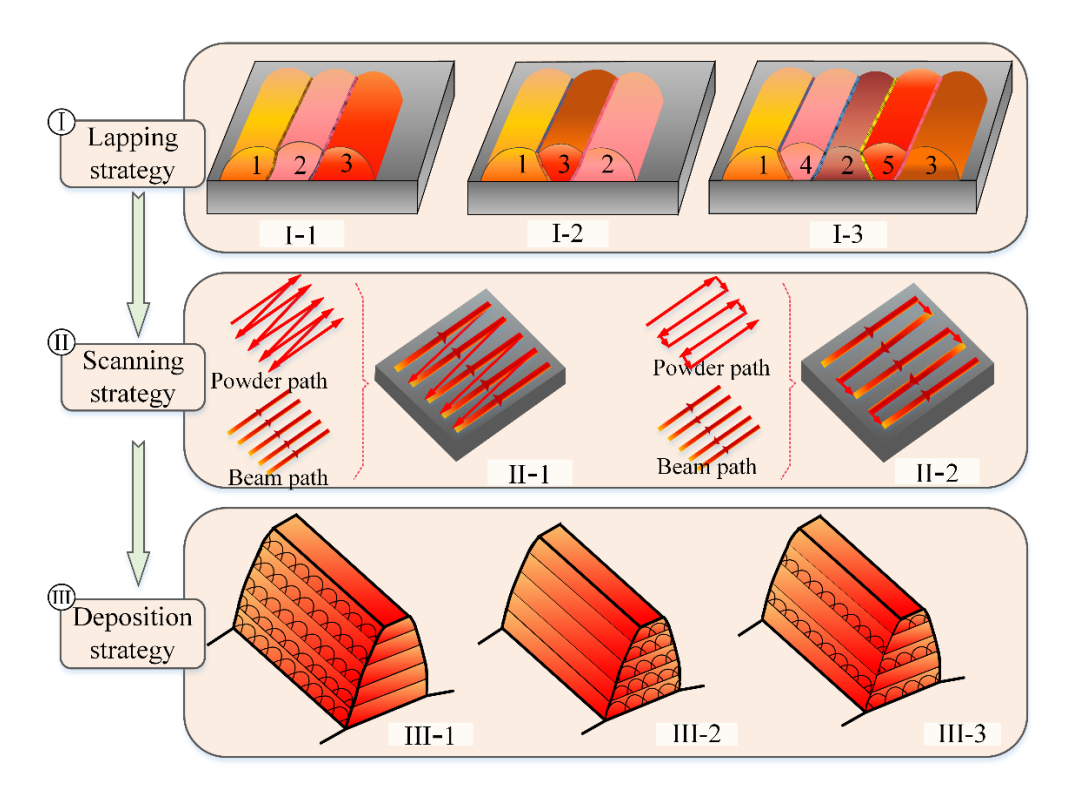


Figure 5. Deposition strategies' optimization of the gear tooth: (I-1) hot lap joint, (I-2) cold lap joint, (I-3) optimized cold strategy, (II-1) co-directional scanning, (II-2) reverse scanning, (III-1) interlayer scanning perpendicular to the axial direction, (III-2) interlayer scanning parallel to the axial direction, (III-3) scanning directions of the two adjacent layers are perpendicular to each other.

2.3. Characterization

Three-dimensional cross-sections were prepared by linear cutting in the vertical scanning direction. The cross-section was ground with SiC sandpapers from 400 to 2000 grit and then polished with diamond polishing paste with the size of 2.5 μ m. The section morphology and geometric characteristics (W, H, h) were obtained by a laser confocal microscope (OLS4000, Japan), as shown in Figure 3.

The phases of the sample image were derived from X-ray diffraction (XRD, X Pertpro) equipped with the Cu-K α radiation at 2.2 kW. The samples were etched with 7 mL HF, 3 mL HNO3, and 5 mL H $_2$ O for 13 s. The microstructure morphology and element composition were obtained by scanning electron microscopy (SEM, ULTRA PLUS). SEM images were obtained by both backscattered electrons (BSE). BSE has the advantage of generating contrast based on atomic number, so it is easy to visualize due to being especially sensitive to boride and carbide precipitates. However, the BSE has a gap in properly distinguished fine Ni-B-Si eutectics with 100 nm thick layers and Ni solid solution dendrite.

The Vickers microhardness tester MH-500 was employed to measure the microhardness from the bottom to the top of the repaired gear teeth. The parameters are the load of 500 gf, the loading time of 10 s, and the distance between the two adjacent test points is 400 μ m. The equipment of friction and wear MFT-4000 was employed for obtaining the wear properties. A GCr15 ball is used for a pair of grinding parts. The friction length is 5 mm, friction time is 40 min, and wear speed is 220 mm/min.

3. Results and Discussion

3.1. Effect of Process Parameters on the Single-Track Quality

Analysis of the results of orthogonal and interaction experiments use the range method. The results and analysis of the orthogonal experiment are given in Figure 6 and Table 4, where I, II, and III represent the average dilution rate values of the three levels of parameters, respectively, K_1 , K_2 , and K_3 represent the average width–height ratio of three levels of

Appl. Sci. 2023, 13, 319 8 of 22

parameters, respectively, and R represents the range. The magnitude of the range directly reflects the degree of influence of the factor on the parameter. Too low β will lead to poor metallurgical bonding between the current layer and the substrate or former coating. While too high dilution β will lead to serious remelting and influence the forming stability. The quality of the cladding layer is better when the dilution ratio is 20–30% [32]. When $\lambda \gg 2$, deposition efficiency is low. When $\lambda < 2$, the molten pool will exhibit high collapse sensitivity [33]. The "Rank" in Table 4 indicates the degree of the factor influence of the four parameters (P, V_S, V_P, Q) on β and λ . Based on the dependent variables β , λ , and the results of the analysis of the range method in Table 4, the order of importance of the effect of each parameter on β is $R_Q > R_{V_S} > R_{V_P} > R_P$, and the order on λ is $R_Q > R_{V_S} > R_P > R_{V_P}$. However, each parameter influences β and λ in a different order, it can be concluded that Q and V_S are major factors, and P and V_P are minor factors. The following parameters should be chosen: Q = 7 L/min, $V_S = 10 \text{ mm/s}$, $V_P = 0.8 \text{ r/min}$, P = 380 W, according to the results of the dilution rate range analysis. This situation is not special in orthogonal experiments [34]. The effects of different levels of each parameter on β and λ are fitted in Figure 6. From Figure 6, the Q ranges from 7 to 7.5 L/min, the V_s ranges from 8 to 10 mm/s, the V_P ranges from 6 to 7 r/min, and the P of 380 W is suitable for both β and λ . So, interaction experiments were established and analyzed to further optimize the uniform parameters on β and λ .

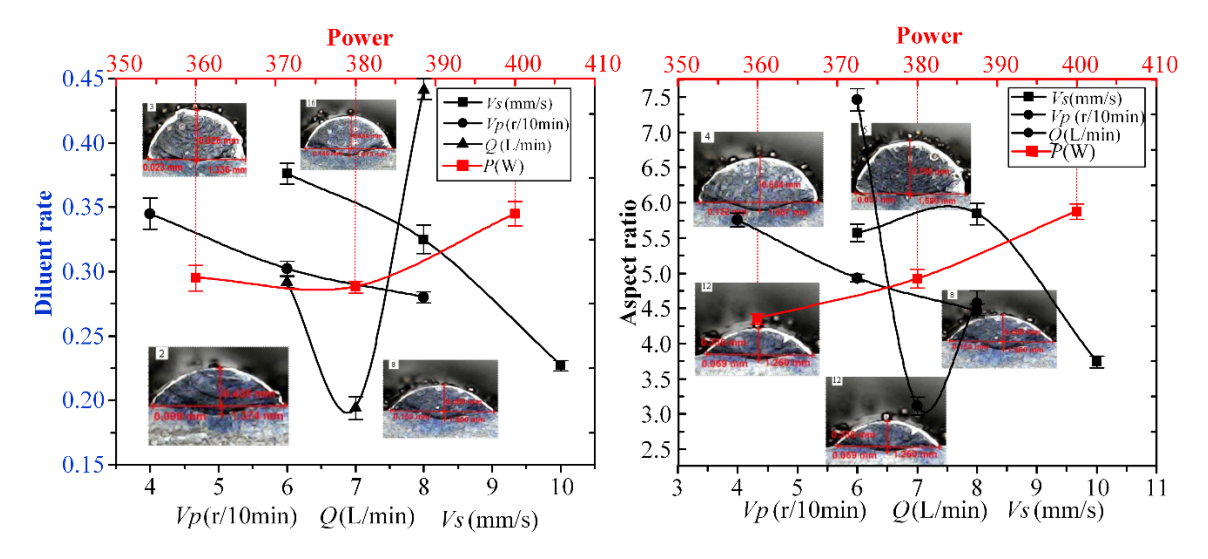


Figure 6. Analysis of the orthogonal experiment.

Table 4. The results of the orthogonal experiment.

	P (W)	V _S (mm/s)	V _P (r/min)	Q (L/min)	Rank
I	0.295	0.376	0.345	0.292	
II	0.288	0.325	0.302	0.194	The rank of β
III	0.345	0.227	0.280	0.441	$R_Q > R_{V_S} > R_{V_P} > R_P$
R	0.057	0.150	0.065	0.247	~ 3 .
K_1	4.353	5.572	5.757	7.462	
K_2	4.922	5.840	4.932	3.115	The rank of λ
K_3	5.877	3.740	4.462	4.574	$R_Q > R_{V_S} > R_P > R_{V_P}$
R	1.52	2.10	1.29	4.35	

As shown in Table 5, C_1 and C_2 represent the average dilution rate value of the two levels of parameters, respectively. The degree of influence of the interaction experiment on each parameter is $Q > Q \times V_S > P > P \times V_P > Q \times P > V_S \times P > Q \times V_P > V_P > V_S \times V_P > V_S \times V_P > V_S$. The parameter of $Q \times V_S$ and $Q \times V_S$ and $Q \times V_S$ have very obvious interactions and the interaction of $Q \times P$ is not obvious, as shown in Figure 7. The coatings with a dilution rate of 20% exhibited good bonding properties, according to the previous study [32]. Therefore,

Appl. Sci. 2023, 13, 319 9 of 22

level 2 for Q, level 2 for V_S , level 1 for P, and level 1 for V_P , were selected in this study. The optimized parameters for Ni60 on 20CrMnTi are Q of 7.5 L/min, V_S of 9.5 mm/s, V_P of 0.6 r/min, and P of 370 W.

Table 5	Results of the interactive experiment.	

Level	Q	V_S	$Q \times V_S$	P	$Q \times P$	$V_S imes P$	V_P	$Q \times V_P$	$V_S \times V_P$	$P \times V_P$
C_1	0.309	0.256	0.272	0.243	0.265	0.262	0.259	0.253	0.258	0.266
C_2	0.204	0.257	0.240	0.270	0.248	0.251	0.253	0.260	0.254	0.247
R	0.105	-0.001	0.032	-0.027	0.017	0.011	0.006	-0.007	0.004	0.019

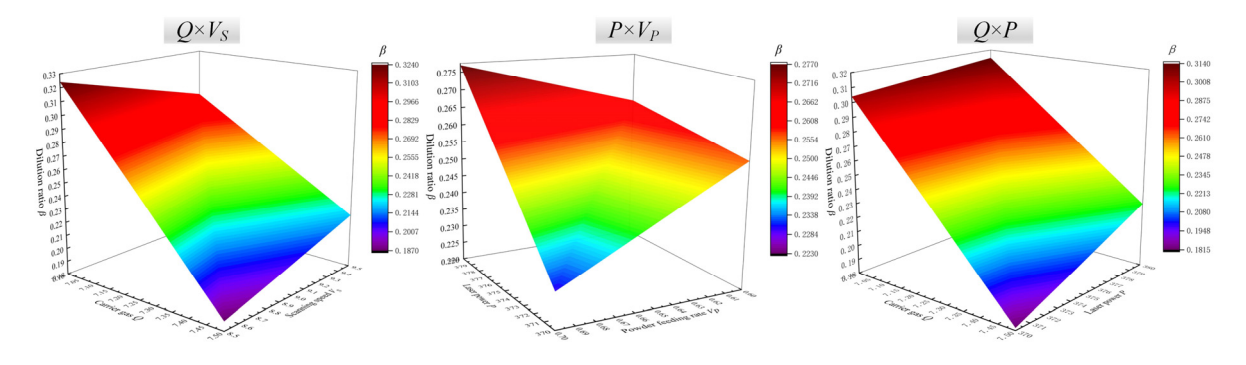


Figure 7. The interaction of the four parameters.

3.2. Effect of Lap Rate on Forming Stability

3.2.1. Effect of Overlap Rate on Forming Stability

As shown in Figure 8, the overlap rate (δ) decreases as D increases. When D is 0.6 mm and 0.8 mm, the overlap joint of each coating layer is extremely obvious with the stacking phenomenon and forms the inclined surface. This phenomenon is the opposite direction of the sequence of cladding. There is an overlap gap between the channels instead of the inclined surface when the center distance is 1.2 mm and 1.4 mm. Overlap is an important reference parameter for the center distance; when δ is greater than 20% and close to 20%, it is easy to achieve a flat cladding surface [33,35]. When D is 1.0 and 1.2 mm, the surface flatness of the deposition layer is better. When D is 1.0 mm, the overlap rate $\delta_{1.0}$ is 32.43%. When D is 1.2 mm, the overlap rate $\delta_{1.2}$ is 15.49. Both $\delta_{1.0}$ and $\delta_{1.2}$ approach 20%. According to the linear change of diluent and center distance, $\delta_{1.1}$ is calculated to be 23.96% in the optimized scope. When D is 1.1 mm, it can make up for the insufficiency. In summary, the center distance is selected as 1.1 mm in this study.

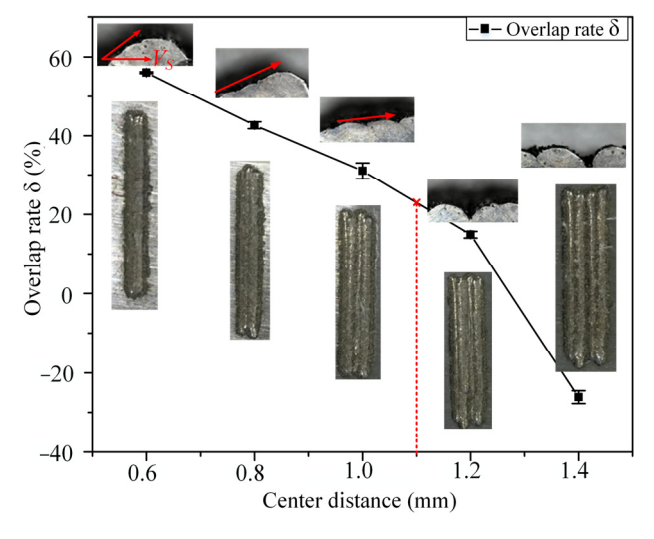


Figure 8. Transverse overlapping.

Appl. Sci. 2023, 13, 319 10 of 22

3.2.2. Effect of Z-Increment on Forming Stability

Figure 9 shows cross-sectional images of the six layers with lifting amounts (ΔZ) of 0.30 mm, 0.28 mm, and 0.26 mm, respectively. When ΔZ is 0.30 mm, the two sides of the cross-section of the cladding layer are relatively vertical, and the theoretical height is the closest to the actual height. The height error between the actual height and the theoretical height is 0.33%, which is much lower than 6.4% (Figure 9b) and 7.6% (Figure 9c). Figure 9b,c also have defects such as irregularity and increasing cladding width, which causes inclination of the cladding side. In general, the most appropriate ΔZ is 0.30 mm. Figure 9b,c are both in the case of ΔZ less than 0.30 mm. Thus, the lifting amount is less than the actual ΔZ . As shown in Figure 9d, the lifting amount is determined to ensure that the area of the rectangle ABCD is equal to the area of the first cladding layer. Thus, the area of the remelted part is equal to the sum area of the area AOD and the area BQC. When the ΔZ is relatively small, the second layer of cladding layer AMB becomes the cladding layer A'M'B', and the remelting area changes from the area ONQ to the area PNR. The remelting area is much larger than the sum area of the A'PD and the B'RC. The excess cladding layer will first lead to the extension on both sides. As the number of cladding layers increases, the extension will become more obvious, forming the inclination of both sides of the cladding layer, as shown in Figure 9b,c. The second effect is to reduce the utilization rate of the powder. Therefore, there is a large amount of un-melted or micromelting powder on the surface and edge of cladding paths, and even embossment appears, resulting in irregularities on both sides of the cladding layers in Figure 9b,c. When the ΔZ is small, the distance from the laser head becomes smaller. Therefore, when the next layer of LC is performed, the energy density will increase. This part of the increased energy is refracted and part of it is used for remelting. If there is remaining energy, the remaining powder can be utilized, so the actual height in Figure 9b is 6.4% higher than the theoretical height. Figure 9c is considered to increase the energy consumption of the remelting area, and the utilization rate of large powder is lower, resulting in a low energy utilization rate. Therefore, the actual height is 7.6% lower than the theoretical height.

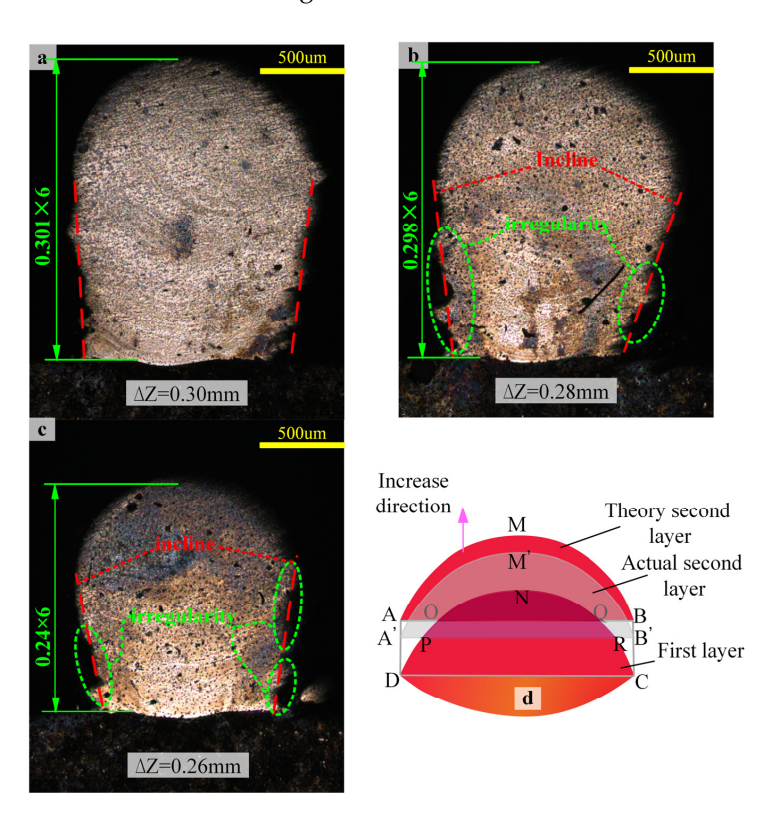


Figure 9. Micrograph of the cross-section of the longitudinal lap.

Appl. Sci. 2023, 13, 319 11 of 22

3.3. Effect of Remanufacturing Strategies on the Quality

3.3.1. Effect of Lapping Strategies on the Multi-Tracks Single Layer

Morphologies of deposition layers under strategies I-1, I-2, and I-3 are shown in Figure 10. From Figure 10, the degree of surface flatness follows strategy I-1 > strategy I-2 > strategy I-3. The optimized cold strategy I-3 is the worst in surface flatness and the surface sticky powder is serious. The first reason is that LC is a process of rapid melting and rapid solidification. Strategy I-3 gives enough cooling time to the previous cladding path. When the cladding path was clad again, the location of the remelted zone changed. The previous cladding path largely played the role of the substrate, and then the height of the cladding was raised, and the remelting expansion zone was raised too. The flatness of the cold lap would be very poor, as shown in Figure 10b,c. The more thoroughly the cooling is raised, the more obvious the phenomenon that the adjacent cladding path is raised, and the more uneven the surface is. The other reason is that the cooling of the previous cladding path, the substrate area of the LC, needs to be larger, and then the energy consumption is relatively larger, resulting in low powder utilization and more powder scattered on the surface. Therefore, the cold lap sticky powder is also more serious.

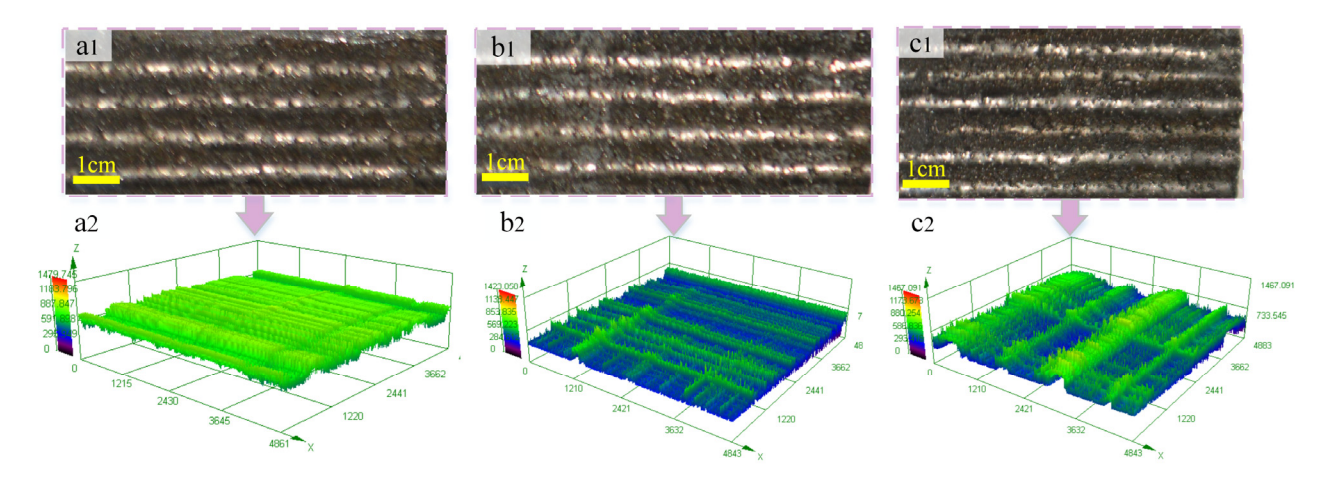


Figure 10. Morphologies of deposition layers under different lapping strategies: (a) Strategy I-1, (b) Strategy I-2, (c) Strategy I-3.

3.3.2. Effect of Scanning Strategies on the Multi-Tracks Multi-Layers

Figure 11 depicts the morphologies of deposition of nine layers under scanning strategies II-1 and II-2. A common phenomenon in Figure 11(a1,b1) is bulging and collapsing at both ends of the scanning route. It can be seen from the cladding path map. After beginning a path or completing a path, the coaxial powder feeding nozzle would be lifted a certain height in the Z-axis direction stopping briefly at the path endpoint. At this time, the powder will be continuously ejected from the nozzle (the laser is off). It is equivalent to the simultaneously proceeding powder-feeding LC and preset powder-feeding LC at both endpoints. Each layer will be slightly higher at the endpoints. When multilayer LC is carried out, the height difference of each layer will be superposed to form a bulge. On the other hand, when the nozzle stays at the endpoint of a just finished path, the continuous carrier gas and protective gas blowing to the molten pool will generate an impact effect on the liquid cladding layer, and the coating material will also bounce or fly out during the process, resulting in less powder entering the molten pool. Then, the liquid surface of the cladding layer will collapse under the action of gravity and surface tension. When multilayer LC was carried out, the collapse of each layer would be superposed to form an inclined surface at the end face. The obvious phenomenon is that the bulge and collapse are serious in the same directional scanning; the paper [36] also explains this phenomenon. The metal powder, carrier gas, and protective gas at both ends of the route have a larger amount of accumulation, so there is more powder to support bulging and more gas to

Appl. Sci. 2023, 13, 319

support collapsing in the same directional scanning. Another reason is that the end point of one path adjacent to the starting point of the next route is on the same end face of the cladding layer in the reverse scanning. The collapse and bulge depressions alternately appear so the defects of collapse and bulge are complemented. In summary, the end face defects of the reverse scanning surface are not obvious.

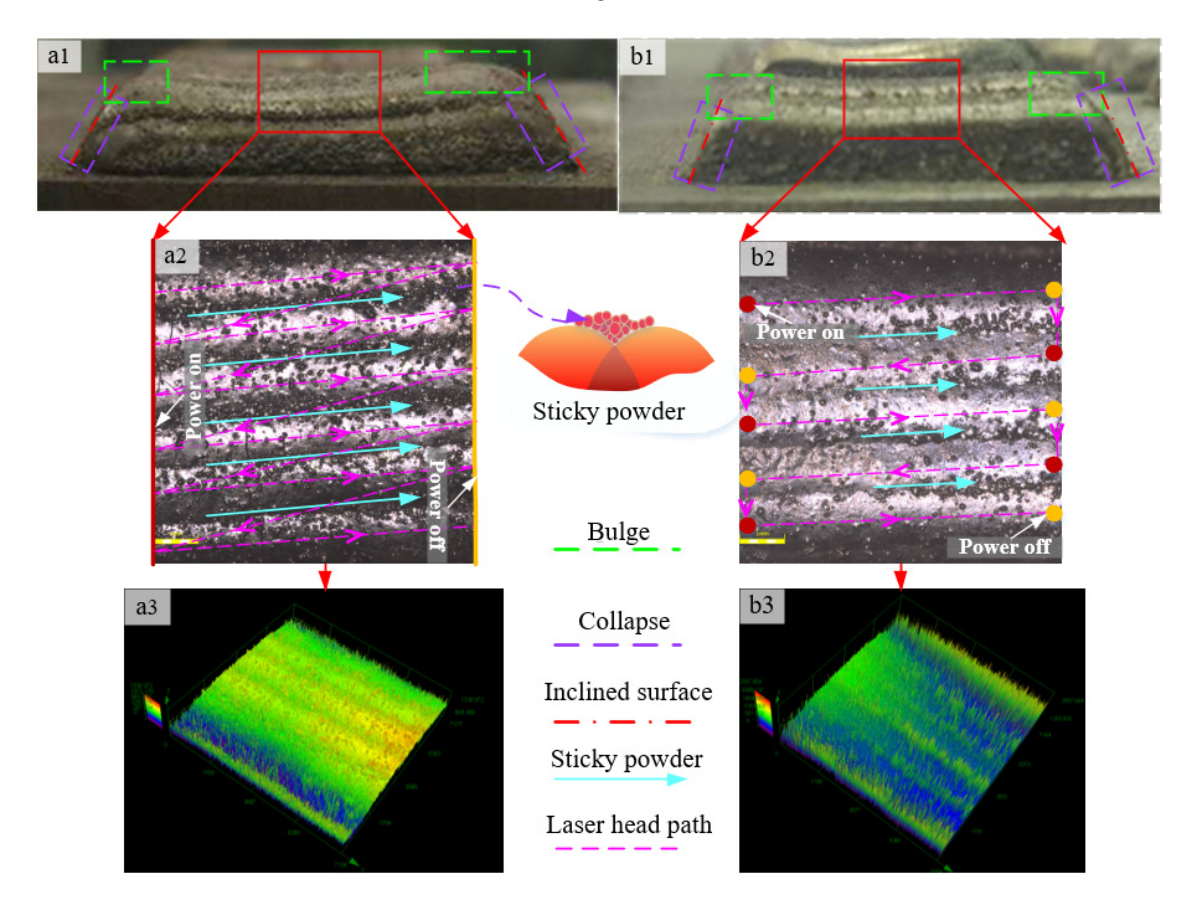


Figure 11. Morphologies of deposition layers under different scanning strategies: **(a1)** Strategy II-1, **(a2)** enlarged view of a1, **(a3)** 3D morphology of a2, **(b1)** Strategy II-2, **(b2)** enlarged view of b1, **(b3)** 3D morphology of b2.

Compared with the scanning in the same direction as shown in Figure 11(a2,a3,b2,b3), the other phenomenon is that the middle part cladding layer of the reverse scanning is relatively flat. The powder-sticking phenomenon of the cladding layer in the same direction is also serious. From the scanning path, in the same direction when a path is completed, the nozzle will turn back to the next path starting point. The nozzle produces an oblique path on the cladding layer, as shown in Figure 11(a2). A lot of redundant powder falls on the surface first, resulting in the powder sticking phenomenon due to the residual temperature of the cladding layer. The redundant powder secondly results in the cladding surface being uneven. Then, residual powder in the middle part would be clad in the next LC. However, the reverse powder feeding path will find the nearest starting point for the next scanning path with no redundant powder spray on the surface of the cladding. To sum up, scanning in the reverse direction has a flatter surface and less sticky powder.

3.3.3. Effect of Deposition Strategies on the Deposition Stability

Morphologies of deposition layers under deposition strategies III-1, III-2, and III-3 are shown in Figure 12. A crucial problem of error accumulation in inter-layer scanning affects the quality of the cladding layer, as shown in Figure 12d. In the actual overlap process, an unfilled zone between the tracks would be formed. When the LC of inter-layer overlap is carried out, errors would be accumulated. As shown in Figure 12(a1–c1), the deposition

Appl. Sci. 2023, 13, 319 13 of 22

layer fabricated by strategy III-3 has the best smoothness, followed by strategy III-2. The deposition layer fabricated by strategy III-1 is rough. As shown in Figure 12(a2-c2), the processing route of the X-direction is the shortest. This path results in the absolute coincidence of corresponding trajectories in each layer, and then the error is absolute accumulation. As shown in Figure 12(a3), the endpoints are continuous in the same direction, so the error of bulges or collapses is absolute accumulation. During the deposition process according to strategy III-1, the proportion of endpoints with bulge or collapse to a single track is large. This phenomenon leads to an increase in the frequency of thermal stress cycles at the endpoints, reducing the bonding properties of the deposited layer to the substrate, and ultimately leading to the generation of cracks [37] (see Figure 12(a1)). As shown in Figure 12(b2), the current deposition layer would be offset after the previous cladding layer was completed. Therefore, although the errors between the two tracks are in the same direction, it was not absolutely accumulated [22], as shown in Figure 12(b3). It is worth noting that the collapse and bulge at the end of deposition layers fabricated by strategy III-2 are more serious. However, this phenomenon is not obvious in Figure 12(c1). Since the deposition direction of each layer is 90 degrees, the error direction is also perpendicular to each other. Therefore, the error accumulation was significantly reduced (see Figure 12(c2)). Moreover, the error and defects at the endpoint of the deposition layer fabricated by strategy III-3 can be compensated, as shown in Figure 12(c3). A residual tensile stress field was formed during LC, and the direction of its maximum value is the same as the scanning direction [38,39]. As the number of layers increases, residual tensile stresses would be accumulated. The direction of the residual tensile stress can be redirected by using strategy III-3, which can effectively reduce the accumulation of residual tensile stress. Therefore, based on the above analysis, strategy III-3 was selected to fabricate the damaged tooth in this study.

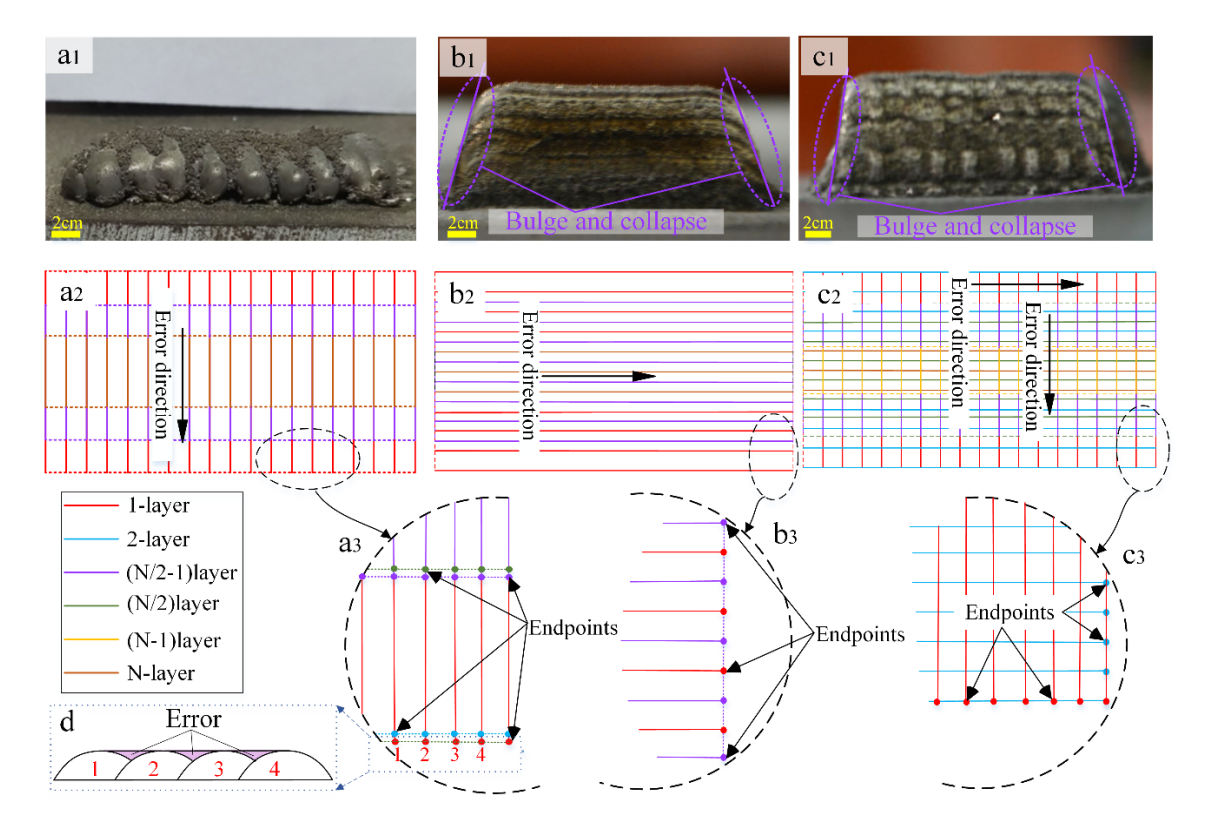


Figure 12. Morphologies of deposition layers under different deposition strategies: (a) Strategy III-1, (b) Strategy III-2, (c) Strategy III-3, (d) Errors owing to incomplete filling.

Appl. Sci. 2023, 13, 319 14 of 22

3.4. Gear Repairing Process

According to the above research, the repair content of the damaged gear is carried out, as shown in Figure 13. The wire-electrode cutting technology was used to produce a flat repair surface which was cleaned with anhydrous ethanol, as shown in Figure 13a. Ni60 powder was dried at 100 °C for 4 h to remove the water vapor, as shown in Figure 13b. Before conducting the repair experiment: P is set through the laser generator; Q and Vp are set through the powder feeder; Vs, δ , ΔZ deposition strategies are set and other control switches (laser on/off, start/stop of powder feeder and protective gas) are set through the Kuka robot as shown in Figure 13c. The actual mode of the LC is converted by robot art software into a language path recognized by the KUKA robot. The path generated by the robot automatically generates two kinds of file codes (dat and src). The dat file mainly generates the coordinate points of the path, and the src file describes the path in detail, as shown in Figure 13d. To prevent the laser head from overrunning, the tracks should be optimized after the tracks were generated, and then the tracks were simulated to verify the feasibility, as shown in Figure 13e. The experimental procedure is shown in Figure 13f. The repair gear tooth has basically been restored to its pre-breakage shape. However, the surface quality of the repaired tooth is rough, and the meshing lines of the tooth are not accurate. It indicates that a molding error exists during LC. The sticky powder is also an unavoidable disadvantage during LC. The secondary machining is significant for forming the smooth surface and accurate meshing lines, as shown in Figure 13g.

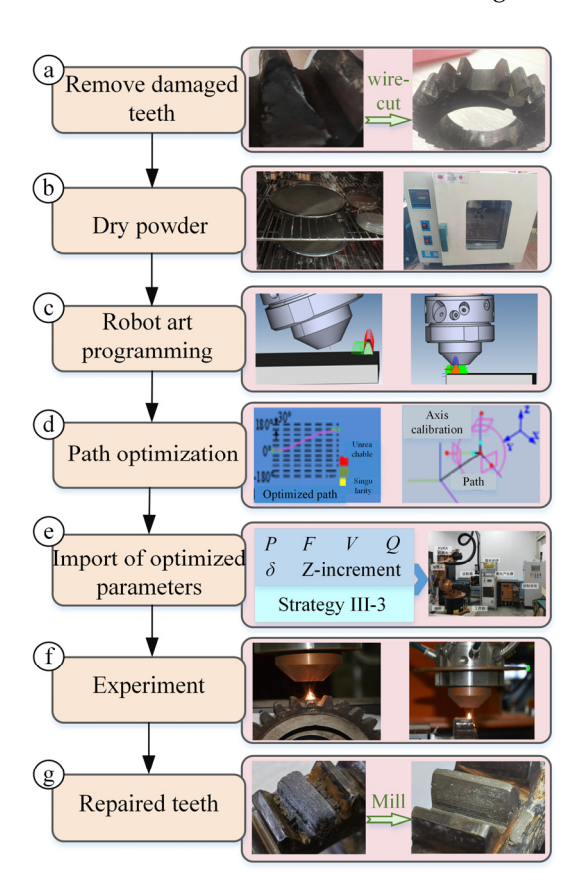


Figure 13. The machining process of gear teeth.

3.5. Microstructure and Mechanical Performance of Repaired Gear

3.5.1. Phase and Microstructure Analysis

The phase in the material is an important indicator that determines its microstructure and mechanical properties [40,41]. As seen in Figure 14, X-ray diffraction (XRD) results show that the repaired gear contains γ -Ni, Ni3B, Cr7C3, Cr23C6, CrB, and Cr5B3; the same compound was also detected in the nickel-based cladding layer [42]. The matrix of the

Appl. Sci. 2023, 13, 319 15 of 22

repaired gear is composed of the γ -Ni phase. All peaks contain Cr-B-C, indicating that various Cr-B-C compounds exist in different lattices. Figure 15a–e indicates representative microstructures from the root to the top of the repaired gear.

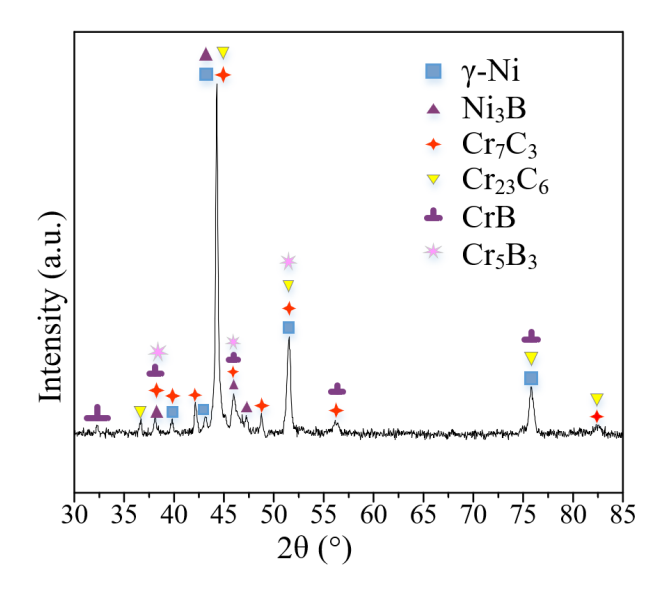


Figure 14. XRD results of the repaired zone.

As shown in Figure 15a, a white bright band presents at the interface, indicating metallurgical bonding was formed between the substrate and cladding layers [18,43]. After the white bright band, many layers of columnar dendrites are formed. The microstructure at the bottom of the repaired zone consists of plane crystal, columnar crystal, and dendrite. When the metal powder is combined with the substrate, it will nucleate and grow on the substrate at a low temperature. At the same time, materials fall off and free from it, so the fine grains and metallurgical bonding are forming, as shown in Figure 15f. After the formation of a fine grain area, there is a large number of high-temperature liquid metal powders deposited. Because of the direction of crystallization during solidification led by the direction of the temperature gradient, the columnar crystal region perpendicular to the bonding surface is found [44], as shown in Figure 15a. During the formation of columnar crystals, new equiaxed crystals may also grow due to local undercooling or free crystals elsewhere. With the solidified front moving inward and upward, the ability of peripheral heat dissipation gradually weakens, and the internal temperature gradient tends to be gentle. Therefore, equiaxed crystals are formed internally to replace large dendrites because of heterogeneous nucleation caused by increased supercooling, as shown in Figure 15a, the same as [18,45]. As the increase in the cladding layers occurs, the transition zone that connects the dense dendrite structure with the precipitate region is shown in Figure 15b, and the enlarged zone is shown in Figure 15g. It can be observed that the microstructure in zone G is finer than the upper and lower parts without precipitates. Considering that there are large amounts of material precipitates in the cladding layer at the top of the transition zone, the exothermic chemical reaction provides a lot of heat for grain refinement. Moreover, the heat released was limited, so grains in the transition zone are refined. After the cladding zone of precipitate-free dendritic structure adjacent substrate, three major morphologies of phases were recognizable in the BSE images: bulk-shaped (see Figure 15c,d), butterfly-or wing-shaped (see Figure 15i,j), and dendritic-shaped (see Figure 15h), the same precipitate having been reported in [30,42,43,46]. From Figure 15a–e, these precipitates have gone through processes from thin to coarse and from variable to less. Figure 15(1–7) is the EDS diagram of the corresponding precipitate, and the DES diagram can specifically characterize the atomic weight percentage and atomic centrifuge content [47]. Point 6 indicates that the cladding layer is composed of crystal structures of columnar Ni and Fe dendrites. Points 2, 3, 4, 5, and 7 indicate that the precipitates are various compounds formed by Cr-B-C. Appl. Sci. 2023, 13, 319

Moreover, the volume of the precipitate and content of the Cr element is increased. The precipitates of points 2, 5, and 7 are all black, and their B atomic percentage fluctuates at 45.30%. The precipitates of points 3 and 4 are all gray, and their B atomic percentage fluctuates at 24.38%. Point 1 shows that Fe and Ni are still the main components at the junction, and the content of Fe, Ni, and B is similar, and the content of Cr, and C is low.

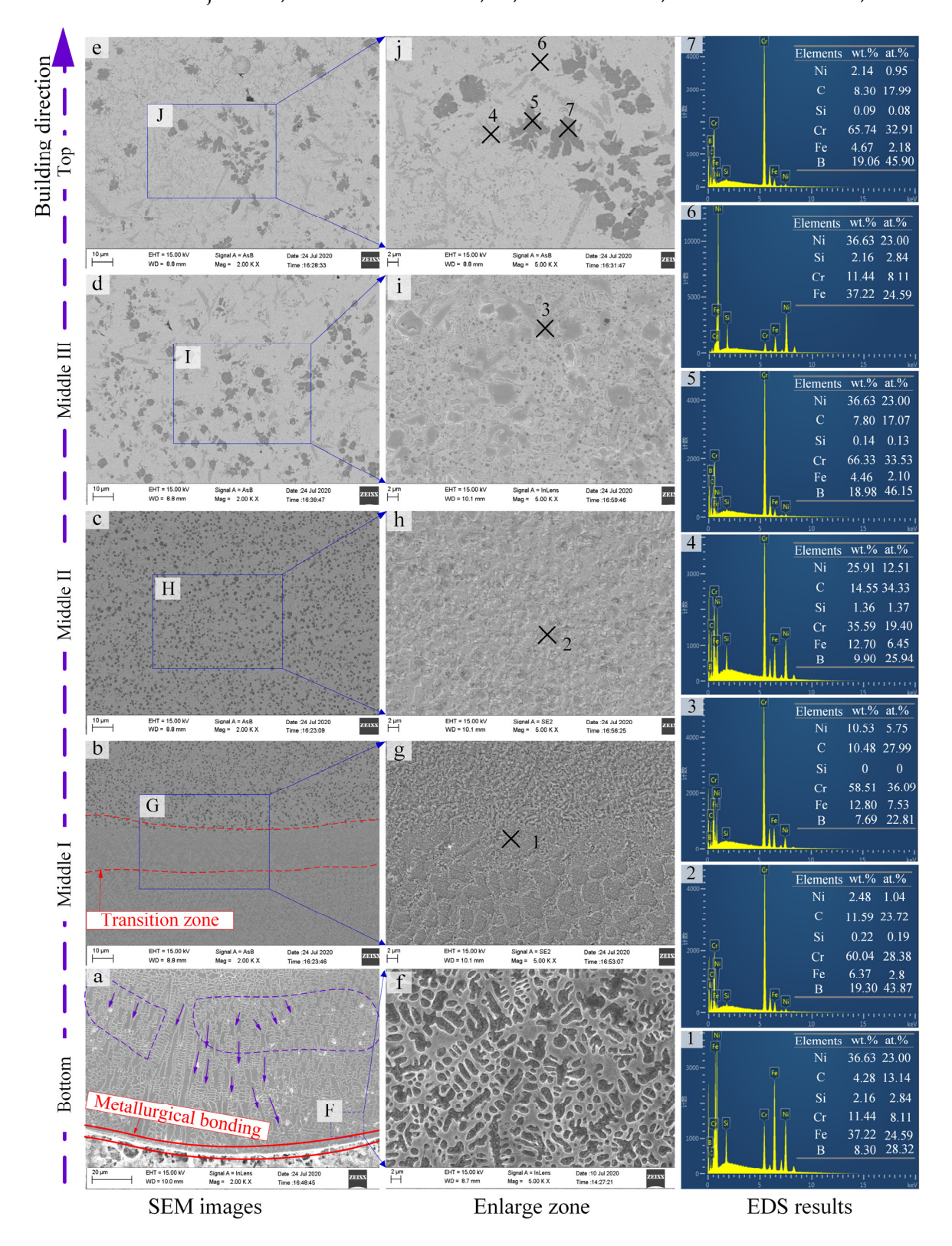


Figure 15. The cross-section micrographs and EDS image of the whole gear teeth.

Appl. Sci. 2023, 13, 319 17 of 22

3.5.2. Microhardness

The main function of the gear is to transfer torque, adjust speed, and adjust direction, so the hardness of the repaired tooth should meet the use requirements. The repaired gear with too high hardness would be excessively worn to transmit unsteadily. The repaired gear with too low hardness will hardly adapt to the complex working conditions. With increased service time, the gear will be very "soft" and easy to wear. Therefore, it is necessary to ensure conditions of the repaired gear are similar to the hardness of other gear teeth. The hardness experimental results are shown in Figure 16; from series 1 to series 3, the data fluctuated in a small range without regular changes in the width direction. From the trend of its fluctuation, there is no obvious rule of hardness in the horizontal direction, and the fluctuation range is small, indicating that the hardness is stable in the horizontal direction. The average hardness of whole gear teeth is 60.63 ± 1.23 HRC. The average hardness of the three series is 60.54 HRC, 60.77 HRC, and 60.58 HRC, indicating that the hardness distribution in the whole cladding area tends to be stable, which is also close to the hardness of the other gear teeth.

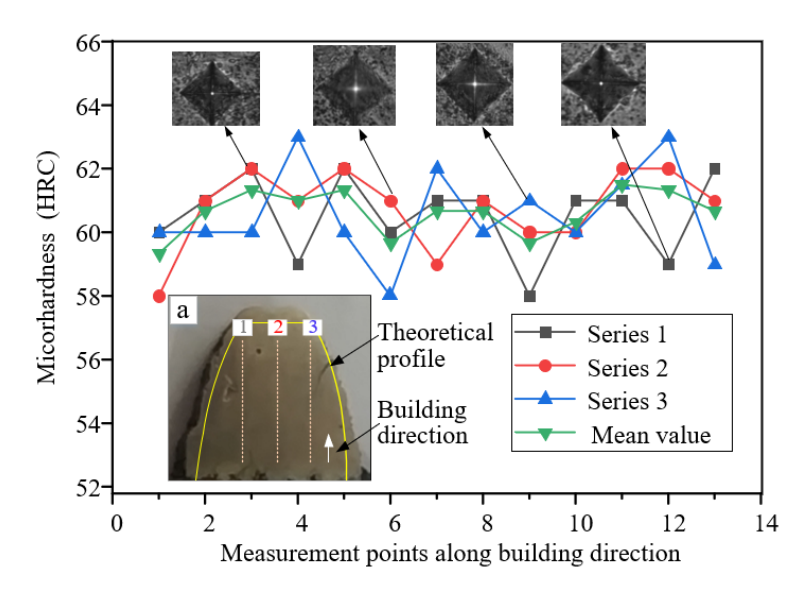


Figure 16. Microhardness and indentation morphologies of the gear teeth.

3.5.3. Wear Performance

Wear performance is one of the most important macroscopic characteristics of the LC layer, which can be evaluated by friction coefficient, volume loss, and worn surface morphology [48–50]. The sample of the frictional wear test was obtained from the repaired gears, as shown in Figure 17. The friction coefficient curves of the substrate and gear teeth are shown in Figure 17. It shows that the friction coefficient is unstable initially, but it attained a stable value after about 10 min. This implies that the friction coefficient of the cladding layer and the substrate are similar. The average friction coefficient of the gear teeth is 0.49, which is 1.06 times of the substrate. Moreover, a stable coefficient of friction allows for the orderly removal of material from the deposited layer, resulting in a robust fatigue life.

The volume loss of substrate and repaired teeth are shown in Figure 18a,b. The section area of repaired teeth is 1674.983 μm^2 and the section area of the substrate is 1675.596 μm^2 . It indicates that wearing capacity is similar. Furthermore, obvious plastic deformation at the edge of the wear track is observed in the wear surface of the 20CrMnTi substrate, as shown in Figure 18(b1,b2). To reveal the wear mechanism, larger magnification optical images of each sample are shown in Figure 19. The large plastic deformation of the substrate would lead to rapid material removal and the formation of abrasive particles. As the slide continues, the abrasive particles micro-cut the substrate, and finally a large groove is

Appl. Sci. 2023, 13, 319 18 of 22

formed on the worn surface, as shown in Figure 19(a1). There would be thermal effects and residual stresses in the deposited layer due to rapid cooling during LC [51,52]. The high and concentrated stress would promote the propagation of micro-cracks, as shown in Figure 19(a3,b3). As shown in Figure 19(a1,a2), the spallings and grooves are precipitated from the worn surface. Therefore, the wear mechanism of sample a is mainly abrasive wear [48]. The substrate peeled off many flakes or scaly flakes, so the worn surface is uneven, as shown in Figure 19(b2). The flakes of the substrate have greater volume, and they are easy to focus on peeling off, especially in the grooves. These flakes with no plastic deformation at the edge and some fatigue cracks are found inside the flakes, indicating that the wear is a typical sign of fatigue spalling. Therefore, the wear mechanism of sample a is mainly adhesive wear and fatigue wear [53,54]. As shown in Figure 19(a3,b3), most of the cracks in the substrate extended very seriously and gathered at the spalling and flakes. The cracks in the cladding layer were few, and their expansion of cracks is not serious. In summary, the wear performance of the cladding layer and the substrate is similar.

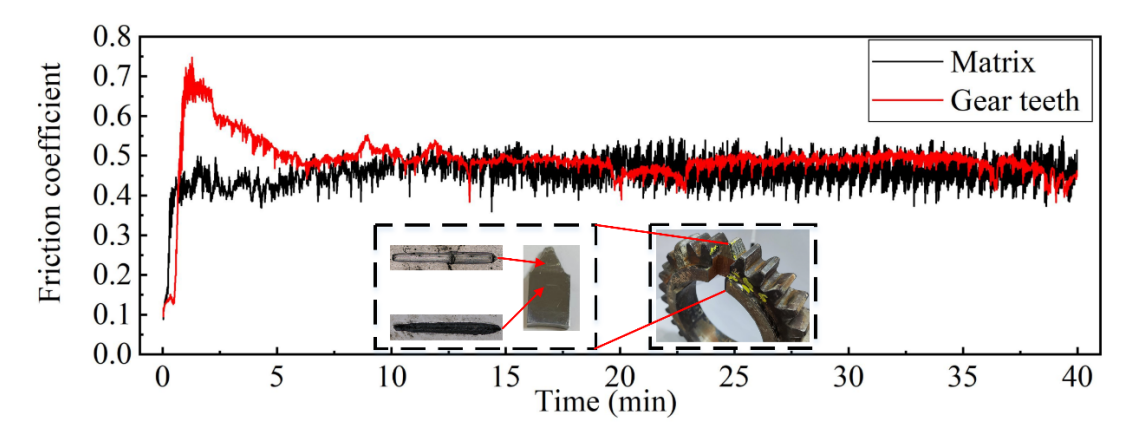


Figure 17. The friction coefficient of the substrate, Ni-based coating.

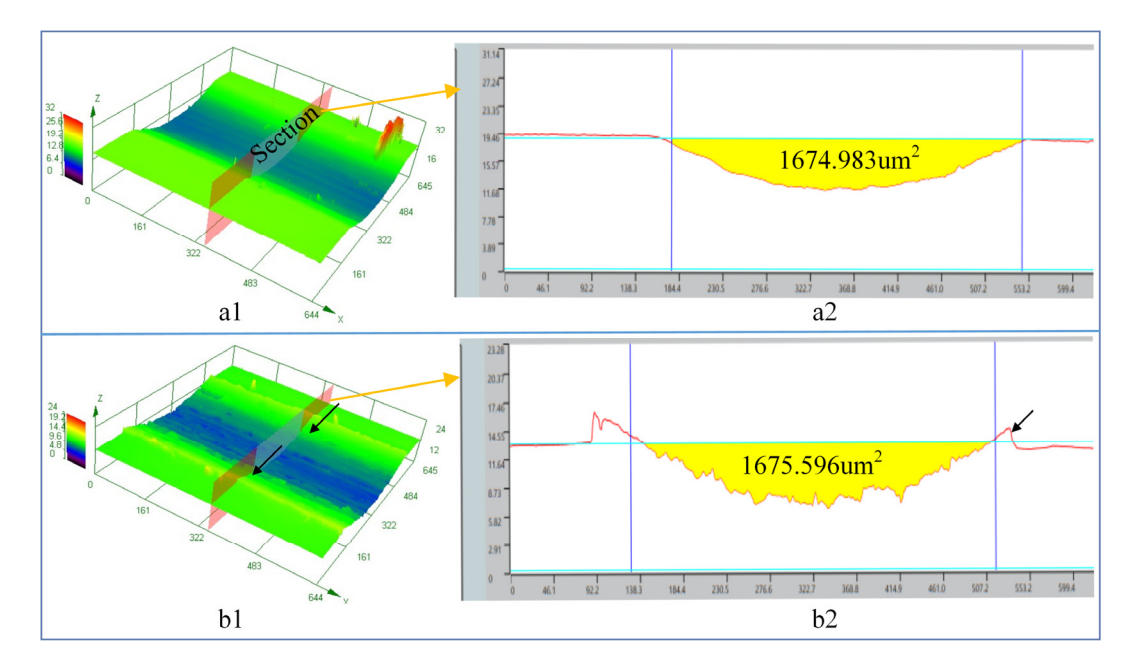


Figure 18. 3D morphologies of wear tracks of (a1) 3D worn surface of Ni60 gear teeth, (a2) corresponding section profile in zone a1, (b1) 3D worn surface of 20CrMnTi substrate, (b2) corresponding section profile in zone (b1).

Appl. Sci. 2023, 13, 319 19 of 22

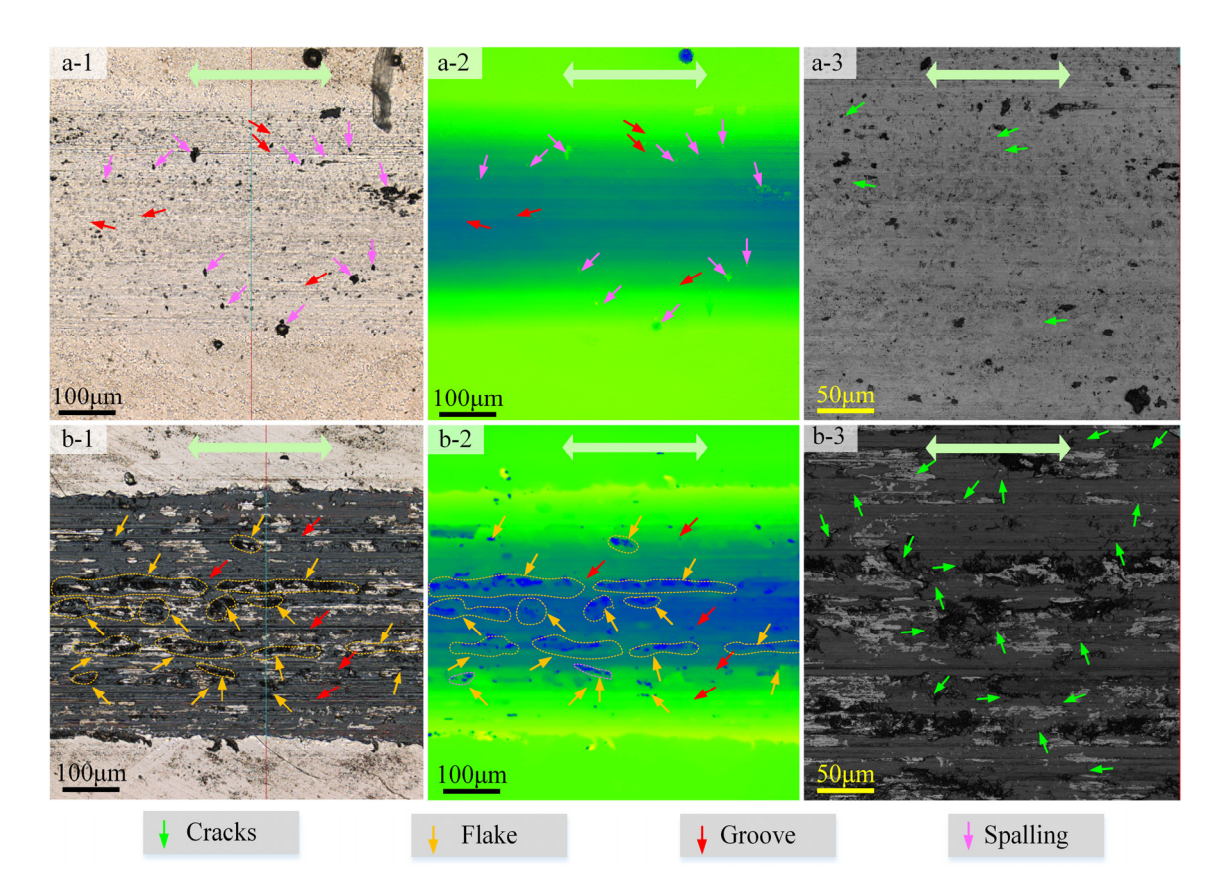


Figure 19. Optical images of worn surfaces (**a-1**) 2D worn surface morphologies of repaired gear teeth, (**a-2**) height graph of a-1, (**a-3**) enlarged view of a-1. (**b-1**) 2D worn surface morphologies of 20CrMnTi substrate, (**b-2**) height graph of b-1, (**b-3**) enlarged view of b-1.

4. Conclusions

This paper systematically studied the repairing process of super gear of 20CrMnTi by LC Ni60 alloy powder. Process parameters' analysis and optimization, deposition strategies' optimization, and performance testing and analysis of repaired teeth were carried out. The conclusions can be drawn up as follow:

- (1) By laser cladding technology, the damaged gear of 20CrMnTi can be repaired with Ni60 powder using the optimal parameters: Orthogonal and interaction experiments were carried out to optimize the parameter of LC Ni60 alloy powder on 20CrMnTi substrates. The optimized process parameters are laser power of 370 W, scanning speed of 9.5 mm/s, powder feeder rate of 0.6 r/min, and carrier gas rate of 7.5 L/min. Moreover, the overlap rate and Z-increment obtained by theoretical calculations and experimental analysis are 23.96%, and 0.3 mm, respectively. Based on the results of the optimization of the deposition strategy, the hot overlap of the same layer (strategy I-1), the reverse scanning method (strategy II-1), and the staggered overlap mode (strategy III-3) can reduce the error accumulation and improve the surface quality and precision.
- (2) The XRD result indicates that the repaired gear contains γ -Ni, Ni3B, Cr7C3, Cr23C6, CrB, and Cr5B3. Moreover, the repaired gear forms a good metallurgical bond with the substrate. The microstructure of the metallurgical bond zone forms plane crystal, columnar crystal, and dendrite in turn. The number of Cr-C-B compounds increases from the dedendum to the addendum. The precipitates exhibit bulk-shaped, butterfly wing-shaped, and dendritic-shaped. Moreover, these precipitates have gone through processes from thin to coarse and from variable to less.
- (3) The hardness of the repaired gear teeth is 60.63 HRC, which is similar to that of other gear teeth. The friction coefficient and volume loss of repaired gear teeth are 0.49

Appl. Sci. 2023, 13, 319 20 of 22

and $1675.596 \ \mu m^2$ respectively, which is similar to that of the substrate. The wear mechanism of the substrate is concluded to be adhesive wear, and the repaired gear is dominated by abrasive wear.

Author Contributions: Conceptualization, C.G. and T.Y.; methodology, Y.Z. and L.C.; software, Y.C.; validation, C.G.; formal analysis, C.G.; investigation, C.G.; resources, T.Y.; data curation, C.G.; writing—original draft preparation, C.G.; writing—review and editing, C.G., Y.Z. and L.C.; visualization, C.G., L.C. and Y.C.; supervision, T.Y.; project administration, C.G.; funding acquisition, T.Y. All authors have read and agreed to the published version of the manuscript.

Funding: This research was funded by the Fundamental Research Funds for the Central Universities (N2003026); 111Project (B16009).

Institutional Review Board Statement: Not applicable.

Informed Consent Statement: Not applicable.

Data Availability Statement: Not applicable.

Acknowledgments: This paper is supported by the Fundamental Research Funds for the Central Universities (N2003026); 111Project (B16009).

Conflicts of Interest: The authors declare no conflict of interest.

References

- 1. Shi, J.; Bai, S.Q. Research on Gear Repairing Technology by Laser Cladding. Key Eng. Mater. 2013, 546, 40–44. [CrossRef]
- 2. Chen, L.; Xie, P.L. Numerical Analysis of Temperature Field in Laser Cladding on Teeth Surfaces of Gear Shaft. *Appl. Mech. Mater.* **2010**, 29–32, 571–576. [CrossRef]
- 3. Wang, S.; Liu, Q. Development Status and Prospect of Remanufacturing of Used and Waste Machine Tools. *Surf. Eng. Remanufacturing* **2018**, 102, 15–18.
- 4. Morgado, T.; Valente, C. Development Status of LASER Cladding and the New Metallic Alloys. *Preprints* **2018**, 2018050417. [CrossRef]
- González-Barrio, H.; Calleja-Ochoa, A.; Lamikiz, A.; de Lacalle, L.N.L. Manufacturing Processes of Integral Blade Rotors for Turbomachinery, Processes and New Approaches. Appl. Sci. 2020, 10, 3063. [CrossRef]
- 6. Xu, L.; Song, Z.; Li, M.; Li, F.; Guo, J.; Gao, M. Self-Grinding Silage Knife Strengthened with Ni–Wc Alloy Prepared by Laser Cladding. *Appl. Sci.* **2021**, *11*, 10236. [CrossRef]
- 7. Iovanas, D.M.; Dumitrascu, A.E. Comparative Reliability Analysis of Milling Teeth Manufactured by Conventional Cutting Processes and Laser Cladding. *Appl. Sci.* **2022**, *12*, 7133. [CrossRef]
- 8. Wang, K.; Zhang, Z.; Xiang, D.; Ju, J. Research and Progress of Laser Cladding: Process, Materials and Applications. *Coatings* **2022**, 12, 1382. [CrossRef]
- 9. Yan, X.L.; Dong, S.Y.; Xu, B.S.; Cao, Y. Progress and Challenges of Ultrasonic Testing for Stress in Remanufacturing Laser Cladding Coating. *Materials* **2018**, *11*, 293. [CrossRef]
- 10. Wang, Z.; Jiang, X.; Yang, G.; Liu, W.; Song, B. Remanufacturing Oriented Multilayer Cladding Morphology Prediction Using a New Second Order Fitting Method. *Environ. Sci. Pollut. Res.* **2022**. [CrossRef]
- 11. Graf, B.; Gumenyuk, A.; Rethmeier, M. Laser Metal Deposition as Repair Technology for Stainless Steel and Titanium Alloys. *Phys. Procedia* **2012**, *39*, 376–381. [CrossRef]
- 12. Lant, T.; Robinson, D.L.; Spafford, B.; Storesund, J. Review of Weld Repair Procedures for Low Alloy Steels Designed to Minimise the Risk of Future Cracking. *Int. J. Press. Vessel. Pip.* **2001**, *78*, 813–818. [CrossRef]
- 13. Sun, W.; Chu, X.; Lan, H.; Huang, R.; Huang, J.; Xie, Y.; Huang, J.; Huang, G. Current Implementation Status of Cold Spray Technology: A Short Review. *J. Therm. Spray Technol.* **2022**, *31*, 848–865. [CrossRef]
- 14. Zhou, S.; Zhao, Y.; Wang, X.; Li, W.; Chen, D.; Sercombe, T.B. Enhanced Corrosion Resistance of Ti-5 Wt.% TiN Composite Compared to Commercial Pure Ti Produced by Selective Laser Melting in HCl Solution. *J. Alloys Compd.* **2020**, 820, 153422. [CrossRef]
- 15. Hua, L.; Zhou, R.D. Damage and Fatigue Life Evaluation for Laser Cladding Remanufactured Wheel. *Adv. Mater. Sci. Eng.* **2022**, 2060564. [CrossRef]
- 16. Chen, L.; Yu, T.; Guan, C.; Zhao, Y. Microstructure and Properties of Metal Parts Remanufactured by Laser Cladding TiC and TiB2 Reinforced Fe-Based Coatings. *Ceram. Int.* **2022**, *48*, 14127–14140. [CrossRef]
- 17. Jiang, X.; Tian, Z.; Liu, W.; Tian, G.; Gao, Y.; Xing, F.; Suo, Y.; Song, B. An Energy-Efficient Method of Laser Remanufacturing Process. *Sustain. Energy Technol. Assess.* **2022**, 52, 102201. [CrossRef]
- 18. Chen, W.J.; Chen, H.; Li, C.C.; Wang, X.; Cai, Q. Microstructure and Fatigue Crack Growth of EA4T Steel in Laser Cladding Remanufacturing. *Eng. Fail. Anal.* **2017**, *79*, 120–129. [CrossRef]

Appl. Sci. 2023, 13, 319 21 of 22

19. Wei, A.; Tang, Y.; Tong, T.; Wan, F.; Yang, S.; Wang, K. Effect of WC on Microstructure and Wear Resistance of Fe-Based Coating Fabricated by Laser Cladding. *Coatings* **2022**, *12*, 1209. [CrossRef]

- 20. Wang, C.; Gao, Y.; Wang, R.; Wei, D.; Cai, M.; Fu, Y. Microstructure of Laser-Clad Ni60 Cladding Layers Added with Different Amounts of Rare-Earth Oxides on 6063 Al Alloys. *J. Alloys Compd.* **2018**, 740, 1099–1107. [CrossRef]
- Cao, Y.-B.; Zhi, S.-X.; Qi, H.B.; Zhang, Y.; Qin, C.; Yang, S.-P. Evolution Behavior of Ex-Situ NbC and Properties of Fe-Based Laser Clad Coating. Opt. Laser Technol. 2020, 124, 105999. [CrossRef]
- 22. Yu, T.; Zhao, Y.; Sun, J.; Chen, Y.; Qu, W. Process Parameters Optimization and Mechanical Properties of Forming Parts by Direct Laser Fabrication of YCF101 Alloy. *J. Mater. Process. Technol.* **2018**, 262, 75–84. [CrossRef]
- 23. Verdi, D.; Múnez, C.J.; Garrido, M.A.; Poza, P. Process Parameter Selection for Inconel 625-Cr3C2 Laser Cladded Coatings. *Int. J. Adv. Manuf. Technol.* **2017**, 92, 3033–3042. [CrossRef]
- 24. Ocelík, V.; Oliveira, U.; De Boer, M.; De Hosson, J.T.M. Thick Co-Based Coating on Cast Iron by Side Laser Cladding: Analysis of Processing Conditions and Coating Properties. *Surf. Coatings Technol.* **2007**, 201, 5875–5883. [CrossRef]
- Xie, M. Process Study and Profile Prediction on Laser Cladding of Titanium Alloys. Doctoral Thesis, Dalian University of Technology, Dalian, China, 2014.
- Li, Y.; Dong, S.; He, P.; Yan, S.; Li, E.; Liu, X.; Xu, B. Microstructure Characteristics and Mechanical Properties of New-Type FeNiCr Laser Cladding Alloy Coating on Nodular Cast Iron. J. Mater. Process. Technol. 2019, 269, 163–171. [CrossRef]
- 27. Zhang, X.; Chen, H.; Xu, L.; Xu, J.; Ren, X.; Chen, X. Cracking Mechanism and Susceptibility of Laser Melting Deposited Inconel 738 Superalloy. *Mater. Des.* **2019**, *183*, 108105. [CrossRef]
- 28. Zhao, Y.; Guan, C.; Chen, L.; Sun, J.; Yu, T. Effect of Process Parameters on the Cladding Track Geometry Fabricated by Laser Cladding. *Optik* **2020**, 223, 165447. [CrossRef]
- 29. Yu, T.; Sun, J.; Qu, W.; Zhao, Y.; Yang, L. Influences of z -Axis Increment and Analyses of Defects of AISI 316L Stainless Steel Hollow Thin-Walled Cylinder. *Int. J. Adv. Manuf. Technol.* **2018**, *97*, 2203–2220. [CrossRef]
- 30. Yu, T.; Yang, L.; Zhao, Y.; Sun, J.; Li, B. Experimental Research and Multi-Response Multi-Parameter Optimization of Laser Cladding Fe313. *Opt. Laser Technol.* **2018**, *108*, 321–332. [CrossRef]
- 31. Zhang, Q.M.; Liu, X.M.; Sun, N.; Guan, Z.Z. Fundamental Investigation on Overlapping Coating Formed by Broad-Beam Powder Feeding Cladding. *Jinshu Rechuli/Heat Treat. Met.* **2001**, *26*, 25.
- 32. Hemmati, I.; Ocelik, V.; Csach, K.; De Hosson, J.T.M. Microstructure and Phase Formation in a Rapidly Solidified Laser-Deposited Ni-Cr-B-Si-C Hardfacing Alloy. *Metall. Mater. Trans. A* **2014**, *45*, 878–892. [CrossRef]
- 33. Ocelík, V.; Nenadl, O.; Palavra, A.; Hosson, J.T.M. On the Geometry of Coating Layers Formed by Overlap. *Surf. Coat. Technol.* **2014**, 242, 54–61. [CrossRef]
- 34. Guo, S.; Chen, Z.; Cai, D.; Zhang, Q.; Kovalenko, V.; Yao, J. Prediction of Simulating and Experiments for Co-Based Alloy Laser Cladding by HPDL. *Phys. Procedia* **2013**, *50*, 375–382. [CrossRef]
- 35. Zhang, Z.D.; Dan, J.M.A. Determining Overlapping Ratio of Laser Cladding Based on Reverse Engineering. *Mach. Des. Manuf.* **2016**, *8*, 118–120. [CrossRef]
- 36. Zhao, Y.; Yu, T.; Sun, J.; Chen, L.; Chen, Y. Effect of Laser Cladding on Forming Microhardness and Tensile Strength of YCF101 Alloy Powder in the Different Full Lap Joint Modes. *J. Alloys Compd.* **2020**, 820, 150230. [CrossRef]
- 37. Köhler, H.; Partes, K.; Kornmeier, J.R.; Vollertsen, F. Residual Stresses in Steel Specimens Induced by Laser Cladding and Their Effect on Fatigue Strength. *Phys. Procedia* **2012**, *39*, 354–361. [CrossRef]
- 38. Narayanan, A.; Mostafavi, M.; Pirling, T.; Kabra, S.; Lewis, R.; Pavier, M.J.; Peel, M.J. Residual Stress in Laser Cladded Rail. *Tribol. Int.* **2019**, *140*, 105844. [CrossRef]
- 39. Tamanna, N.; Crouch, R.; Kabir, I.R.; Naher, S. An Analytical Model to Predict and Minimize the Residual Stress of Laser Cladding Process. *Appl. Phys. A* **2018**, *124*, 202. [CrossRef]
- 40. Chen, L.; Yu, T.; Xu, P.; Zhang, B. In-Situ NbC Reinforced Fe-Based Coating by Laser Cladding: Simulation and Experiment. *Surf. Coat. Technol.* **2021**, 412, 127027. [CrossRef]
- 41. Zhao, Y.; Yu, T.; Guan, C.; Sun, J.; Tan, X. Microstructure and Friction Coe Ffi Cient of Ceramic (TiC, TiN and B 4 C) Reinforced Ni-Based Coating by Laser Cladding. *Ceram. Int.* **2019**, 45, 20824–20836. [CrossRef]
- 42. Yinghua, L.; Xuelong, P.; Jiacai, K.; Yingjun, D. Improving the Microstructure and Mechanical Properties of Laser Cladded Ni-Based Alloy Coatings by Changing Their Composition: A Review. *Rev. Adv. Mater. Sci.* **2020**, *59*, 340–351. [CrossRef]
- 43. Yu, J.; Sun, W.; Huang, H.; Huang, Y. Study on the Deformation Control and Microstructures of Thin-Walled Parts Repaired by Laser Cladding. *Coatings* **2020**, *10*, 369. [CrossRef]
- 44. Cheng, J.; Xing, Y.; Dong, E.; Zhao, L.; Liu, H.; Chang, T.; Chen, M.; Wang, J.; Lu, J.; Wan, J. An Overview of Laser Metal Deposition for Cladding: Defect Formation Mechanisms, Defect Suppression Methods and Performance Improvements of Laser-Cladded Layers. *Materials* 2022, *15*, 5522. [CrossRef] [PubMed]
- 45. Wang, K.; Chang, B.; Lei, Y.; Fu, H.; Lin, Y. Effect of Cobalt on Microstructure and Wear Resistance of Ni-Based Alloy Coating Fabricated by Laser Cladding. *Metals* **2017**, *7*, 551. [CrossRef]
- 46. Hemmati, I.; Rao, J.C.; Ocelík, V.; De Hosson, J.T.M. Electron Microscopy Characterization of Ni-Cr-b-Si-c Laser Deposited Coatings. *Microsc. Microanal.* **2013**, *19*, 120–131. [CrossRef]
- 47. Sun, Y.; Jin, L.; Gong, Y.; Wen, X.; Yin, G.; Wen, Q.; Tang, B. Experimental Evaluation of Surface Generation and Force Time-Varying Characteristics of Curvilinear Grooved Micro End Mills Fabricated by EDM. *J. Manuf. Process.* **2022**, *73*, 799–814. [CrossRef]

Appl. Sci. 2023, 13, 319 22 of 22

48. Liu, J.; Shi, Y. Microstructure and Wear Behavior of Laser-Cladded Ni-Based Coatings Decorated by Graphite Particles. *Surf. Coat. Technol.* **2021**, *412*, 127044. [CrossRef]

- 49. Chen, L.; Chen, Y.; Chen, X.; Yu, T.; Wang, Z. Microstructure and Properties of in Situ TiC/Ni Functionally Gradient Coatings by Powder-Fed Laser Cladding. *Ceram. Int.* **2022**, *48*, 36789–36801. [CrossRef]
- 50. Boakye, G.O.; Geambazu, L.E.; Ormsdottir, A.M.; Gunnarsson, B.G.; Csaki, I.; Fanicchia, F.; Kovalov, D.; Karlsdottir, S.N. Microstructural Properties and Wear Resistance of Fe-Cr-Co-Ni-Mo-Based High Entropy Alloy Coatings Deposited with Different Coating Techniques. *Appl. Sci.* **2022**, *12*, 3156. [CrossRef]
- 51. Liu, F.; Lin, X.; Yang, G.; Song, M.; Chen, J.; Huang, W. Microstructure and Residual Stress of Laser Rapid Formed Inconel 718 Nickel-Base Superalloy. *Opt. Laser Technol.* **2011**, 43, 208–213. [CrossRef]
- 52. Guo, P.; Zou, B.; Huang, C.; Gao, H. Study on Microstructure, Mechanical Properties and Machinability of Efficiently Additive Manufactured AISI 316L Stainless Steel by High-Power Direct Laser Deposition. *J. Mater. Process. Technol.* **2017**, 240, 12–22. [CrossRef]
- Govindarajan, V.; Sivakumar, R.; Patil, P.P.; Kaliappan, S.; Kumar, T.C.A.; Kannan, M.; Ramesh, B. Effect of Tungsten Carbide Addition on the Microstructure and Mechanical Behavior of Titanium Matrix Developed by Powder Metallurgy Route. Adv. Mater. Sci. Eng. 2022, 2022, 2266951. [CrossRef]
- 54. Liu, H.; Gao, Q.; Man, J.; Li, X.; Yang, H.; Hao, J. Microstructure and Friction Properties of CoCrFeMnNiTix High-Entropy Alloy Coating by Laser Cladding. *Zhongguo Jiguang/Chinese J. Lasers* **2022**, *15*, 4669. [CrossRef] [PubMed]

Disclaimer/Publisher's Note: The statements, opinions and data contained in all publications are solely those of the individual author(s) and contributor(s) and not of MDPI and/or the editor(s). MDPI and/or the editor(s) disclaim responsibility for any injury to people or property resulting from any ideas, methods, instructions or products referred to in the content.